Chapter 6

6.1 Introduction

In the previous chapter, we have demonstrated the effect of replacement of Mn with Fe and Cr on structural, J-T distortion and magnetic properties of $GdMnO_3$. The present chapter describes structure, J-T distortion and magnetic properties of cation deficient $LaMnO_3$. In $La_{1-x}MnO_3$ when x=0 it is referred as LaMnO1 and when x=0.2, it is named as LaMnO2 throughout the chapter. Structure and surface morphology of these samples are elaborated in 6.2. Magnetic properties are discussed in 6.3. Section 6.4 summarizes the important findings of this study.

6.2 Structural and Microstructural Analysis

In this section, I have analysed the XRD patterns to determine the phase. Rietveld refinement of these patterns are undertaken to know structural details including J-T distortion, bond angles and bond lengths. Particle size and morphology of the samples are discussed from SEM data. The role of oxidation state of cation and anion are discussed using the XPS data.

6.2.1 X-ray diffraction: Rietveld refinement and J-T distortion

Figure 6.1 depicts the powder X-ray diffraction patterns of $La_{1-x}MnO_3$ (x=0 and 0.2). The structures of both samples are analyzed by Rietveld refinement method using Fullprof software. Rietveld analysis of XRD data reveals that the structures of both samples are monoclinic with I2/a space group. The observed patterns, the simulated data and their difference patterns are shown as dots, continuous line and the bottom line respectively. The

tick marks above the difference pattern represent the position of the Bragg peak. No additional peak observed in these spectra indicate the absence of impurities in both samples and hence confirm the single phase, monoclinic structure with space group I2/a. While $LaMnO_3$ prepared by sol-gel technique followed by combustion reaction shows hexagonal structure [114], through solid state ceramic route, it exhibits orthorhombic one [115]. However, in the present case, we observe monoclinic structure, I2/a. The refined structural parameters and agreement factors are given in **Table 6.1**. Although the unit cell volume in both samples are almost same, it is found to be less than the bulk value [116]. Further, the refinement parameters enable us to demonstrate a representative structure of the unit cell showing the spatial orientations of MnO_6 octahedra and their positions shown in **figure 6.1**.

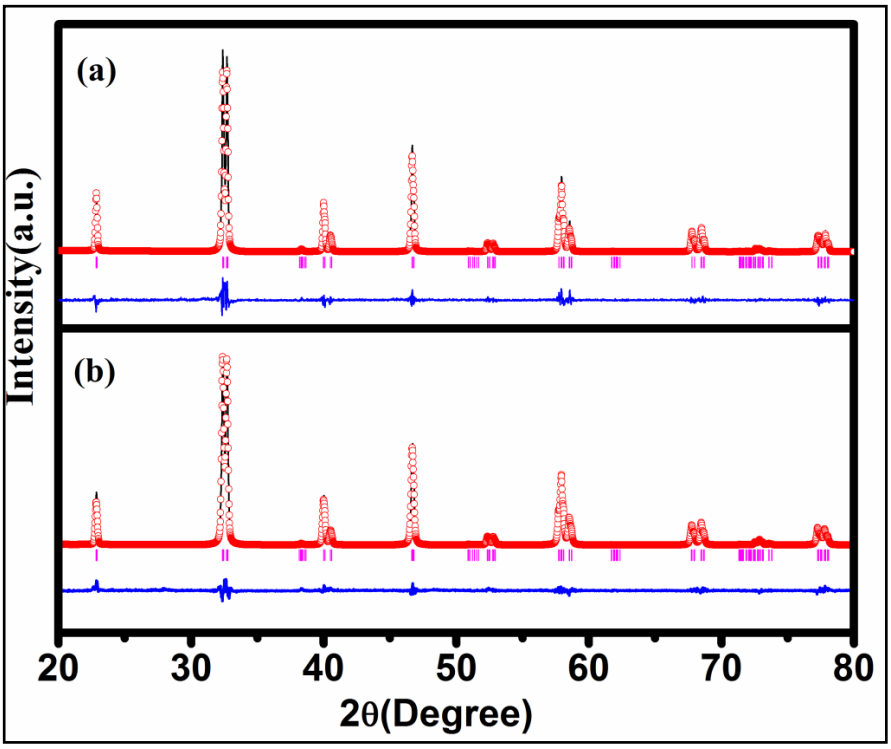

Figure 6.1 *Rietveld refinement of X-ray diffraction (XRD) patterns (a) LaMnO1 and (b) LamnO2 calcined at 900 ˚C.*

Table 6.1 *Structural Parameters of LaMnO1 and LaMnO2 at room temperature (300 K) with monoclinic structure having space group I2/a.*

Parameters	**LaMnO1**	**LaMnO2**
a(Å)	7.775(3)	7.774(3)
b(Å)	5.525(2)	5.528(2)
c(Å)	5.478(2)	5.477(1)
α, β, ϒ	90°,89.24° (3),90°	90°,90.74°(3),90°
V($Å^3$)	235.32	235.41
La(x, y, z)	(0.25,0.4946(8),0)	(0.25,0.496(1),0)
Mn (x, y, z)	(0,0,0)	(0,0,0)
O1 (x, y, z)	(0.25,0,0)	(0.25,0,0)
O2 (x, y, z)	(0,0.200(3),0.265(6)	(0,0.21(7),0.288(2))
χ^2	1.48	1.67
Mn-O1(Å)	1.94	1.94
Mn-O2 (Å)(l)	2.08	1.97
Mn-O2' (Å)(s)	1.94	1.96
Mn-O1-Mn(deg)		
Mn-O2-Mn(deg)	163	165

In MnO_6 octahedra, Mn atoms (purple balls) occupy at the centre of octahedron and 6 oxygen atoms (red balls) are at the corners of octahedraon. These octahedral are tilted to each other, which can be determined from the Mn-O-Mn bond angle and Mn-O-Mn bond length which decides the degrees of tilting of the octahedra and the Jahn–Teller distortion. However, theoretically, lattice distortion and the degrees of tilting of the MnO_6 octahedra can be calculated by using the Gold Schmidt tolerance factor [84]. In a perfect cubic perovskite structure, the length of six Mn-O bonds of the MnO_6 octahedron are equal and the Mn-O-Mn bond angle are of 180 ^{o}. However, in a distorted perovskite structure, the

value of bond angle (Mn-O-Mn) is less than 180 ^{o} with a tolerance factor less than 1.0 [21]and octahedra are tilted with different Mn-O bond length in different directions. The O1 atoms occupy the two apical positions of the MnO_6 octahedra whereas the four equatorial positions are occupied by the O2 atoms which are depicted in **figure 6.2.** The equatorial Mn-

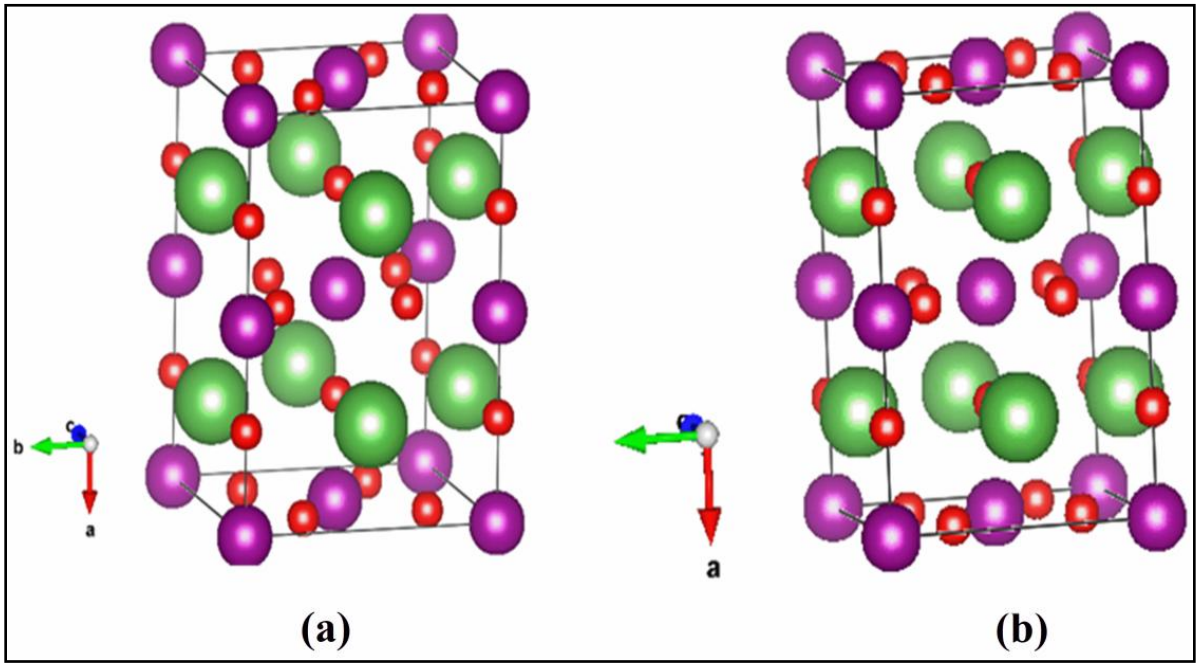

Figure 6.2 *Crystal structure obtained from Rietveld refinement drawn using Vesta software (a) LaMnO1 and (b) LaMnO2.*

O2 bonds have two lengths denoted as long (l) and short (s). In LaMnO1 sample, while the bond lengths of Mn-O1 and Mn-O2 have significant difference, in LaMnO2 sample, no such change is observed. The Mn-O1-Mn bond angle is collinear whereas Mn-O2-Mn bond angles in both the samples are tilted (**Table 6.1**). The large deviation of the bond angle from 180 ^{o}, or in other words, a large value of the tilt angle of two adjacent MnO_6

octahedra signifies a considerable local Jahn-Teller (J-T) distortion supported with the reported literature [98]. Due to a > b > c, one may note that static J-T distortion is superimposed on the monoclinic phase. It is known that monoclinic distortion is a consequence of the buckling and tilting of the MnO_6 octahedra due to geometrical constraints. In an undistorted octahedra, one may expect the average Mn-O bond length is close to the sum of ionic radii of Manganese (r_{Mn}) and Oxygen (r_O) which should be 1.93 Å. Change in Mn-O bond length from 1.93 Å in different directions reveal a strong Jahn–Teller distortion. Evidence of J-T distortion is further quantified by considering bond angle and bond length. For example, the maximum and minimum stretching of Mn-O bonds are found to be 1.83 Å, 2.08 Å in LaMnO1 sample and 1.97 Å, 1.96 Å in LaMnO2 sample (**Table 6.1**) indicating a strong J-T distortion in LaMnO1 sample one. The bond angles between different Mn-O-Mn bonds in two adjacent octahedra have been used to determine the octahedral tilting angle between them. The Mn-O-Mn bond angles between two adjacent octahedra are listed in **Table 6.1**. The coherent J-T distortion can be calculated using the relation,

$$\sigma_{JT}^2 = 1/3\Sigma_i[(Mn\text{-}O)_i\text{-}\langle Mn\text{-}O\rangle] \quad (6.1)$$

where Mn-O and average <Mn-O>i bond lengths are calculated from Rietveld fitting of X-ray diffraction pattern as shown in **Table 6.1** [117]. σ_{JT} is found to be 0.10 and 0.014 for LaMnO1 sample and LaMnO2 sample, respectively. One order magnitude higher in LaMnO1 sample indicates that although both samples crystallize in monoclinic structure, LaMnO2 sample shows a stable monoclinic phase.

6.2.2 Scanning Electron Microscopy:

The field emission scanning electron (FESEM) micrographs of LaMnO1 and LaMnO2 samples shown in **figure 6.3** indicate the agglomeration of the particles. Particle size distribution calculated from the above images using Image-J software are fitted with a Lorentzian distribution function and are shown in the inset of **figure 6.3**. The majority of the agglomerated particles are found to be in the range of 700–800 nm and 300– 400 nm in LaMnO1 and LaMnO2 samples, respectively.

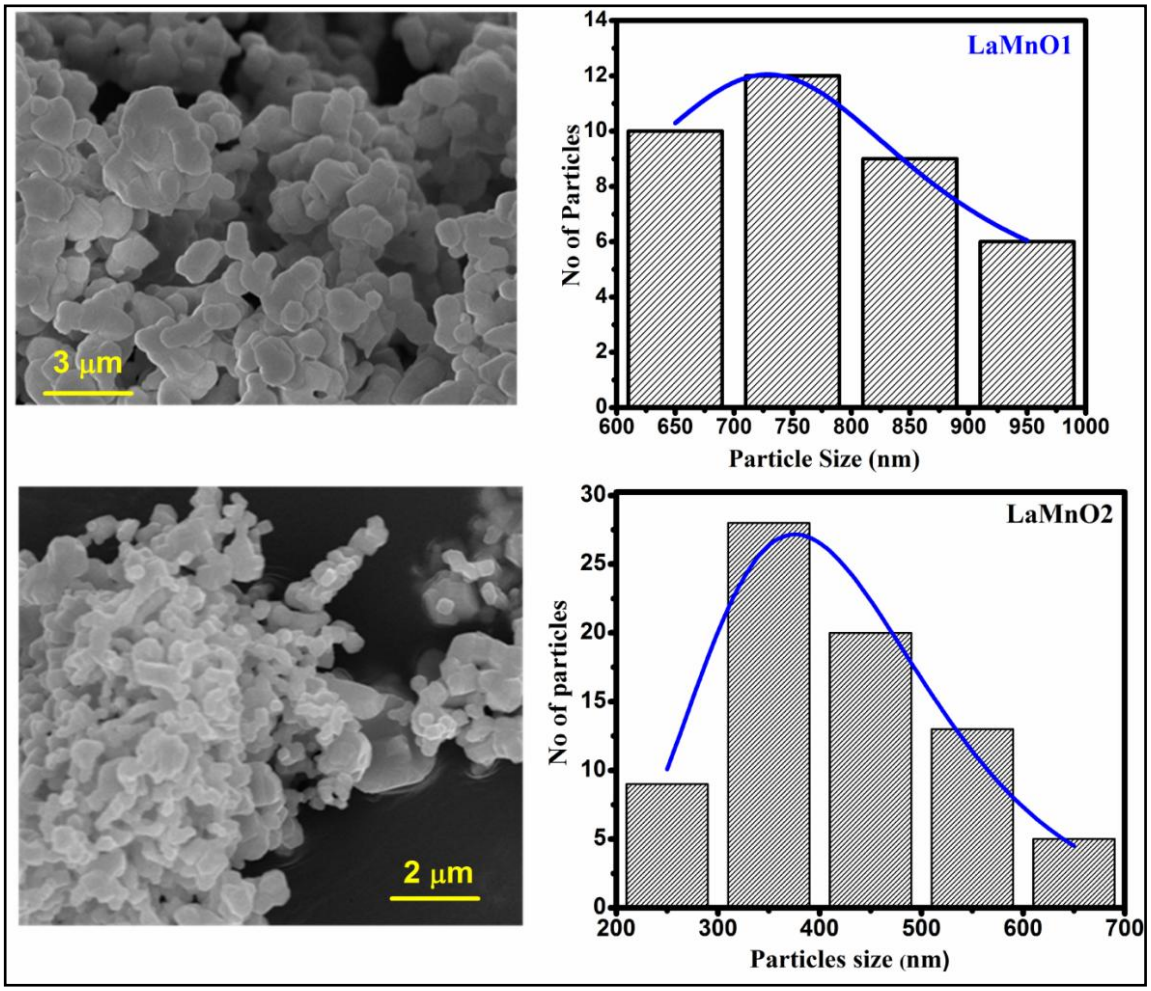

Figure 6.3 (a) *Field emission scanning electron micrographs of LaMnO1 and LaMnO2* ***(b)*** *shows the corresponding particle size distribution histogram.*

6.2.3 X-ray Photoelectron Spectroscopy

To confirm, the oxidation state and oxygen vacancies we have collected the X-ray photoelectron spectra of both samples using Al K_α radiation. The core level binding energies were aligned with the carbon binding energy of 281.4 eV. The Mn^{3+} 2p core level binding energies of both samples show the binding energy of Mn^{3+} state (**figure 6.4(a)**) [22].

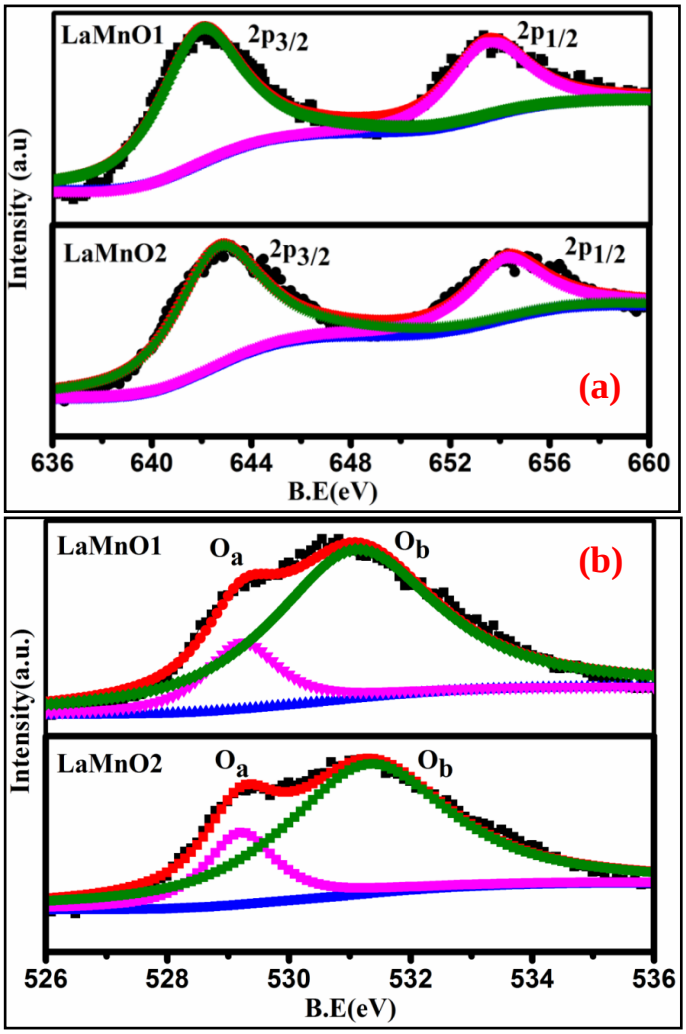

Figure 6.4 (a) *X-ray photoelectron spectroscopy for Mn 2p and* ***(b)*** *O1s of of LaMnO1 and LaMnO2.*

The oxygen 1s core level spectra show the asymmetry around the binding energy at 530 eV in both the samples (**figure 6.4(b)**). The spectra are fitted with two Gaussian peaks, denoted as O_a and O_b, respectively using software XPS peak 4.1 with Shirley background. The O_a peak is ascribed to the lattice oxygen atoms and O_b peak is due to the oxygen vacancies [118]. The area ratio of O_b to O_a is relatively high in LaMnO1 sample (1.14) in comparison to LaMnO2 (0.85).

6.3 Magnetic Properties

To study the magnetic properties of these samples the temperature dependent magnetization, magnetic field dependent magnetization and temperature dependent ac susceptibility are carried out and are discussed in section 6.3.1, 6.3.2 and 6.3.3, respectively.

6.3.1 Temperature dependent magnetization

Figure 6.5 shows the temperature dependent magnetization in field cooled (FC) and zero field cooled (ZFC) protocols in the presence of 100 Oe and 10 kOe external magnetic field. In the ZFC protocol, the sample is cooled to 2 K in zero field and in presence of the measuring field, magnetization is recorded as a function of temperature. However, in the FC protocol, the sample is cooled to 2 K in presence of magnetic field and the magnetization is recorded with increasing temperature applying the same field. The observed magnetic transition is broad due to the broad distribution of nanoparticles as well as inter and intra-particle interactions. With decreasing temperature from 300 K, FC and ZFC magnetization curves split at a temperature denoted as the irreversible temperature, T_{irr}, followed by a rapid increase in magnetization showing a maximum at a critical temperature, T_{max}. T_{max} indicates that the particles can either be spin-glass or

superparamagnetic in nature which have been clarified from ac susceptibility measurement discussed later. The sharp increase in magnetization below room temperature in M_{FC} and M_{ZFC} indicates a paramagnetic to ferromagnetic transition (T_C). It is derived by extrapolating the linear part of the magnetization to zero in a high temperature regime shown in **Figure 6.5.** T_C is found to be 124 K and 219 K in LaMnO1 and LaMnO2 samples at the measuring field of 100 Oe respectively. It has been reported in literature that T_C is different for different structure of $LaMnO_3$. For example, Hernandez et al. observe the T_C at 150 K in hexagonal $LaMnO_3$ [114],

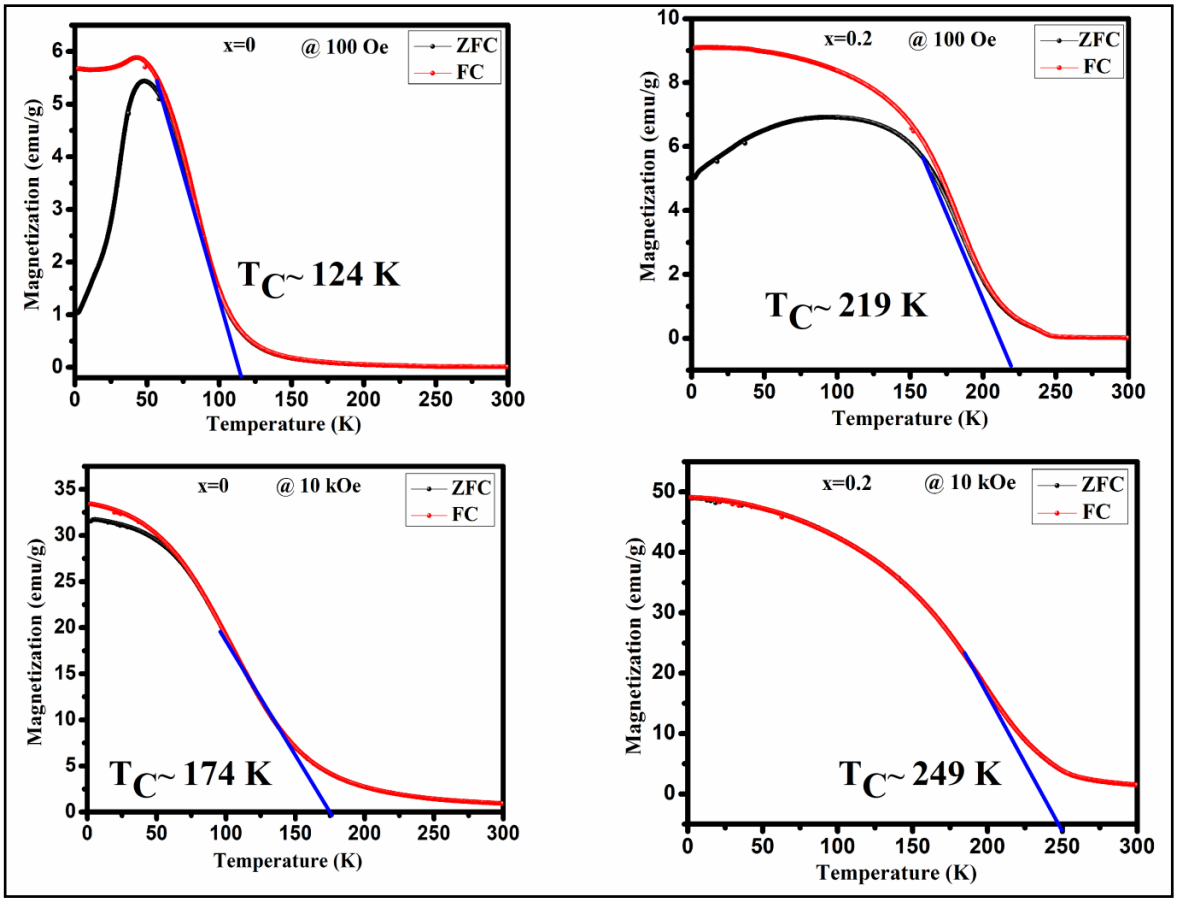

Figure 6.5 (a) *Temperature dependent magnetization under zero field cooling (ZFC) and field cooling (FC) measured at 100 Oe and at 10 kOe for LaMnO1and LaMnO2*

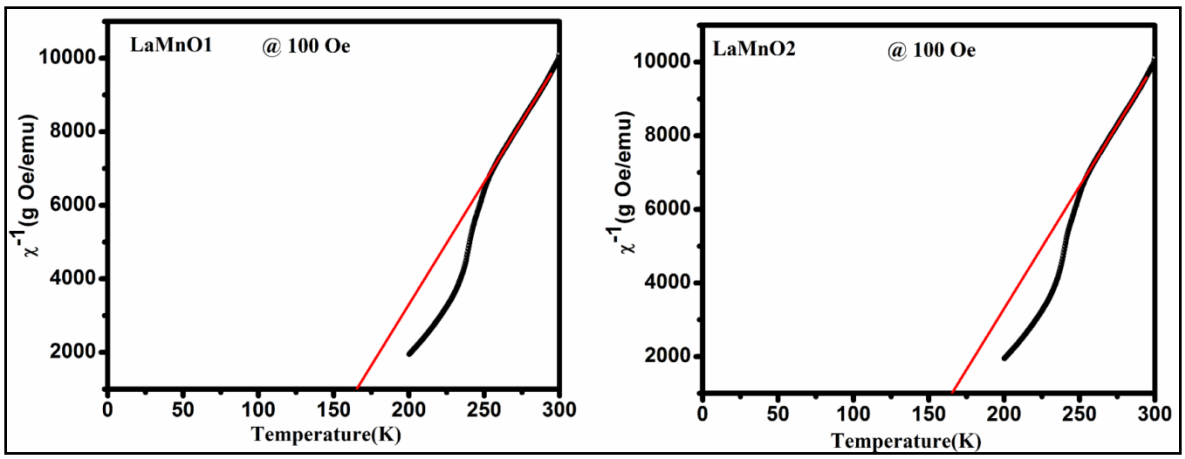

Figure 6.6 *Curie- Weiss law fitting of the LaMnO1 and LaMnO2.*

Brankovic et al. report T_C at 180 K in rhombohedral structure [119] and Ghosh et al. observe at 120 K for orthorhombic one [116]. So far, no report shows T_C in monoclinic phase which approaches more than 200 K in the present study. While monoclinic phase with higher J-T distortion than the rhombohedral structure reported by Ghosh et al. [116]show less T_C, less distorted sample having same monoclinic phase show higher T_C in the present study. With increasing applied magnetic field from 100 Oe to 10 kOe, T_C shifts to higher temperature as expected. The inverse susceptibility ($1/\chi$) versus temperature shown in the **figure 6.6** are fitted with Curie-Weiss law in the paramagnetic region. The positive Weiss constant named as Tp is obtained at 142 K and 230 K after extrapolation of $1/\chi$ to the temperature axis in LaMnO1 and LaMnO2 samples, respectively confirm the ferromagnetic correlation in the ordered state. The difference in Tc obtained from the extrapolation of magnetization in ferromagnetic region and Tp from paramagnetic region is attributed to the small spin clusters which remain present even above Tc. The temperature difference between Tc and Tp decides the size of the spin cluster. The effective magnetic moment calculated from Curie constant is found to be 5.42 μ_B and 4.96 μ_B for LaMnO1

and LaMnO2 samples, respectively. Although the effective magnetic moment in both samples are higher than the theoretical spin only value (4 μ_B), the effective magnetic moment is higher in LaMnO1 sample than LaMnO2 sample. This clearly indicates the role of oxygen vacancies in deciding the magnetic moment. The area ratio of O_b to O_a is relatively high in LaMnO1 sample in comparison to LaMnO2, confirming the high oxygen vacancies and hence high effective magnetic moment.

6.3.2 Field dependent magnetization

Further, we have studied the magnetization behavior with respect to magnetic field in LaMnO1 and LaMnO2 samples at different temperatures such as 300 K, 120 K, 100 K and 5 K (**figure 6.7**). The linear increase in magnetization with magnetic field confirms the paramagnetic phase of both the samples at 300 K. At 120 K, magnetization readily increases at low field and linearly increases up to 70 kOe without showing saturation in LaMnO1 sample. The hysteresis is like S shape. However, in oxygen rich sample, magnetization saturates immediately and shows hysteresis loop of conventional ferromagnetic. Similar behavior has also been found in $LaMnO_3$ prepared by sol-gel technique [120]. We have tabulated maximum magnetization, coercivity (H_c) and remanent magnetization (M_r) at 7 kOe in **Table 6.2**. It is observed that while coercivity is one order magnitude higher in LaMnO1 sample, remenance is almost an order of magnitude higher in LaMnO2 sample, found to be 33 Oe, 2 Oe and 0.001 μ_B, 0.007 μ_B in LaMnO1 and LaMnO2 samples, respectively at 120 K. With further decreasing temperature to 100 K, similar behavior retains although a drastic increase in H_c has been observed at 5 K in both samples. At this temperature, magnetization measured at 70 kOe shows 1 μ_B and 2 μ_B per formula unit in

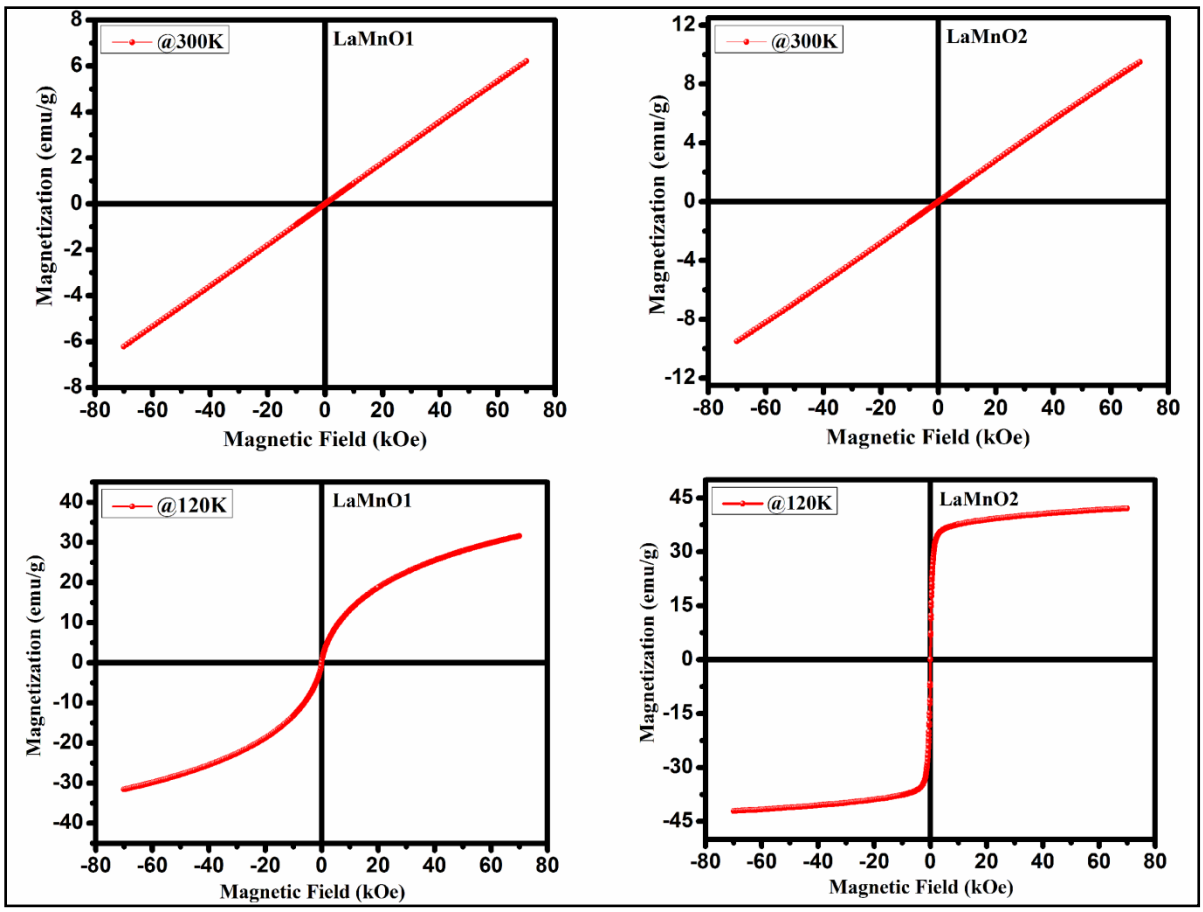
@300K
LaMnO1
Magnetization (emu/g)
Magnetic Field (kOe)
@300K
LaMnO2
Magnetization (emu/g)
Magnetic Field (kOe)
@120K
LaMnO1
Magnetization (emu/g)
Magnetic Field (kOe)
@120K
LaMnO2
Magnetization (emu/g)
Magnetic Field (kOe)

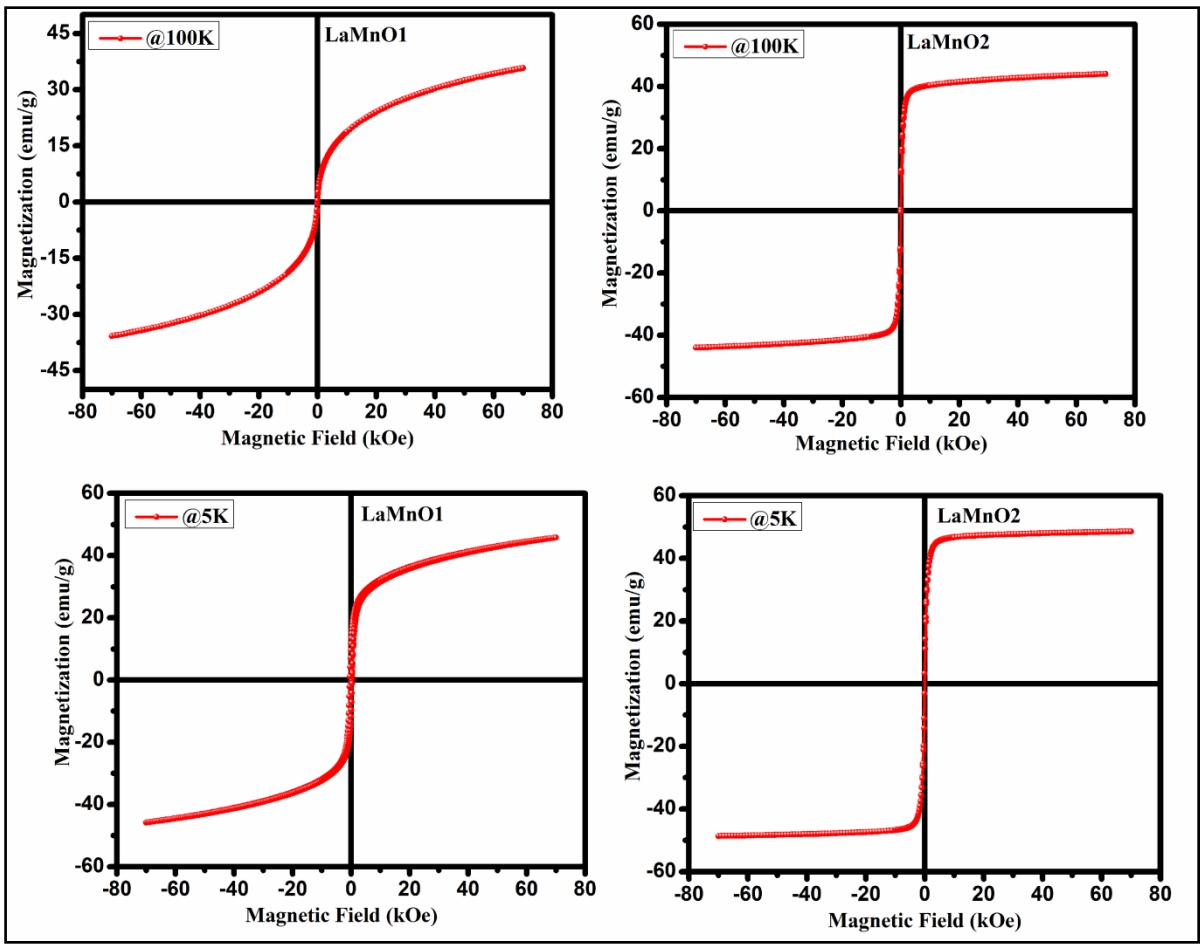

Figure 6.7 *Magnetic field dependent magnetization at 300 K, 120 K, 100 K and 5 K of LaMnO1 and LaMnO2.*

LaMnO1 and LaMnO2 sample, respectively which is almost double the value obtained at 100 K and 120 K. The maximum magnetic moment at 5 K in both samples are within the reported range (0.1–3.0 μ_B) [116],[115],[120]. Although, the maximum magnetic moment calculated at 5 K in both samples are found to be much less than that of the effective moment calculated from paramagnetic region, the less magnetic moment in LaMnO1 sample is attributed to the non saturation of magnetization (**figure 6.7**). Moreover, the large coercivity in LaMnO1 sample further confirms the uncompensated surface spins and weak

FM as corroborated with low T_C observed from magnetization versus temperature measurement.

Table 6.2 Maximium magnetization at 7 T, M_r and H_c for LaMnO1 and LaMnO2 at different temperature.

Temperature	**M_{max} @ 7 T**		**H_C (Oe)**		**M_r (μ_B)**	
	LaMnO1	**LaMnO2**	**LaMnO1**	**LaMnO2**	**LaMnO1**	**LaMnO2**
5 K	1 μ_B	2 μ_B	0.433	0.046	0.08	0.5
100 K	0.7 μ_B	1.55 μ_B	0.036	0.012	0.05	0.02
120 K	0.66 μ_B	1.36 μ_B	0.033	0.002	0.001	0.007

6.3.3 Temperature dependent ac susceptibility

Normally, the broad peak in M versus T and the bifurcation in M_{FC} and M_{ZFC} could occur due to the presence of spin-glass [121], canonical spin-glass [122],[123], cluster-glass [124],[95], or superparamagnetic nature of particles [125],[126]. M_{FC} is not constant with temperature at low temperature i.e. much below T_{max}, which leave out the canonical spin-glass behavior. Thus, the behavior may be due to spin-glass, cluster-glass or superparamagnetic of either interacting or non-interacting nature. We have undertaken an ac susceptibility measurement at low field to discover the dynamics of the system at the time scale of measuring frequency range to get better perceptive of the magnetically-ordered state in these samples. The real part of the linear susceptibility (χ') measured at 3 Oe and at frequencies 3, 31 and 299 Hz is shown in **Figure 6.8**. χ' exhibits a broad peak at T_b/T_f as observed in M_{ZFC} vs temperature plot (**figure 6.4**). With increasing the frequency, the peak position in χ' shifts towards higher temperature (**figure 6.8**). Dispersion behavior

of χ' with frequency is a common feature for spinglass, cluster-glass or superparamagnetic particles.

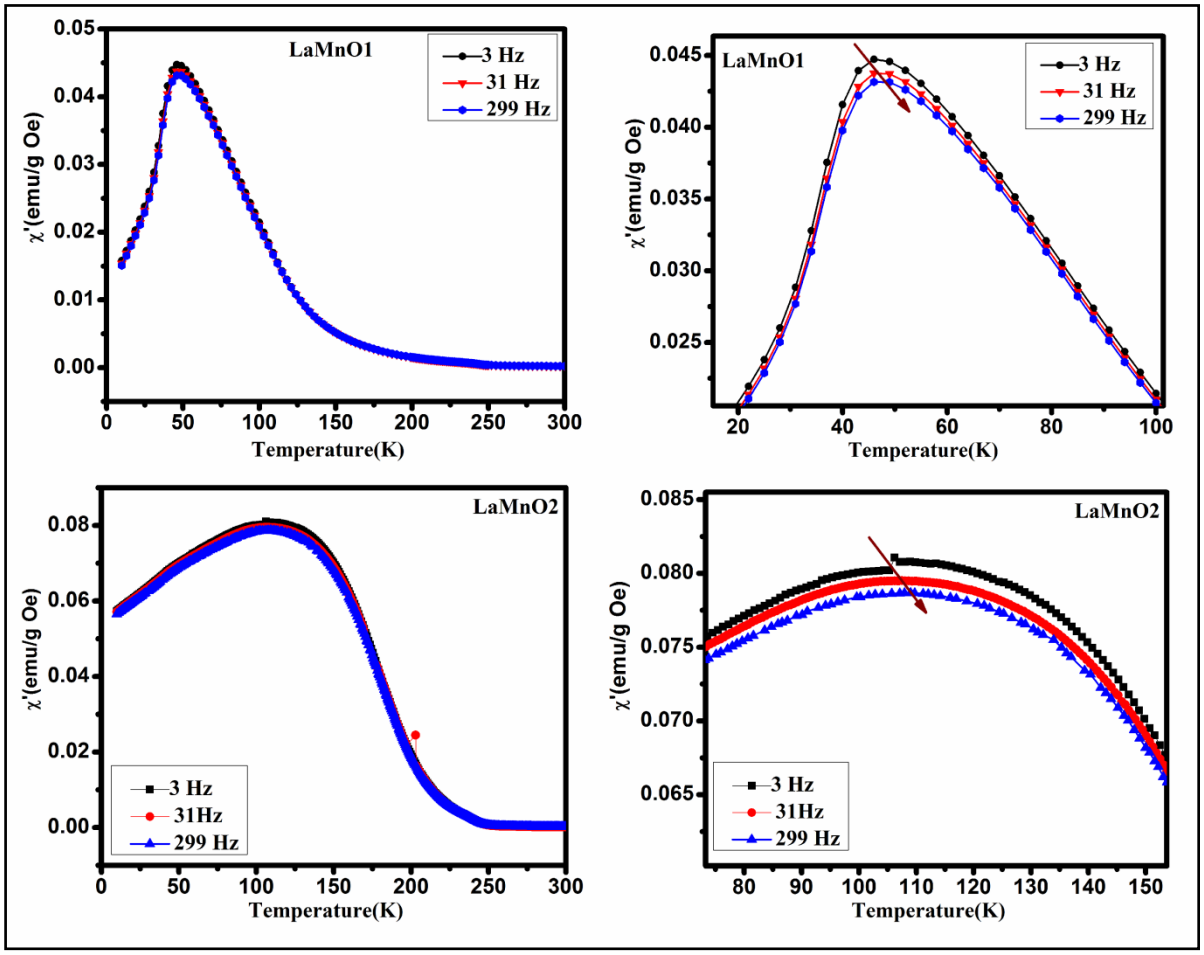

Figure 6.8 *Temperature dependence of the real and imaginary part of ac susceptibility at various frequencies at the 3Oe ac field for LaMnO1 and LaMnO2. The right panel of the respective figure shows the expanded view of the peak shift with increasing frequency.*

To find out the nature of magnetically ordered state the frequency dependence of T_b is fitted with the following empirical relation

$$\phi = \Delta T_B / T_B \Delta (\log\omega) \qquad (6.2)$$

where Δ is the difference in related parameters is the difference in related parameters [121]. The The ϕ are found to be 0.016 and 0.008 for the LaMnO1 and LaMnO2 samples, respectively. Typically, ϕ lies between 0.005–0.08, 0.03– 0.06 and 0.3 for spin-glass [120], for cluster-glass and for noninteracting superparamagnetic particles [127] respectively. The obtained ϕ in both samples matches well with the ϕ of spin-glass not the ϕ of superparamagnetic or cluster-glass. To demonstrate the interaction and its effect on the fluctuation dynamics of the system, we have further evaluated with different phenomenological models like the Neel–Arrhenius, Vogel–Fulcher and Power law [121]. According to Neel–Arrhenius law, for an assembly of noninteracting superparamagnetic particles the relaxation time (τ) is

$$\tau = \tau_0 \exp\left(\frac{Ea}{K_B T}\right) \quad \textbf{(6.3)}$$

where E_a is the average anisotropy (activation) energy barrier which is equal to KV, K is the anisotropy constant and V is the volume of the particle, τ_0 is the time constant corresponding

to the characteristic frequency and k_B is the Boltzmann constant. Fitting our data to Eq. (6.3), τ_0 is found to be $1.20X10^{-47}$ and $6.0X\ 10^{-49}$ in the LaMnO1 and LaMnO2 samples, respectively. However, unphysical values of τ_o observed from Neel–Arrhenius law, further cancel out the possibility of the non-interacting superparamagnetic nature of the particles.

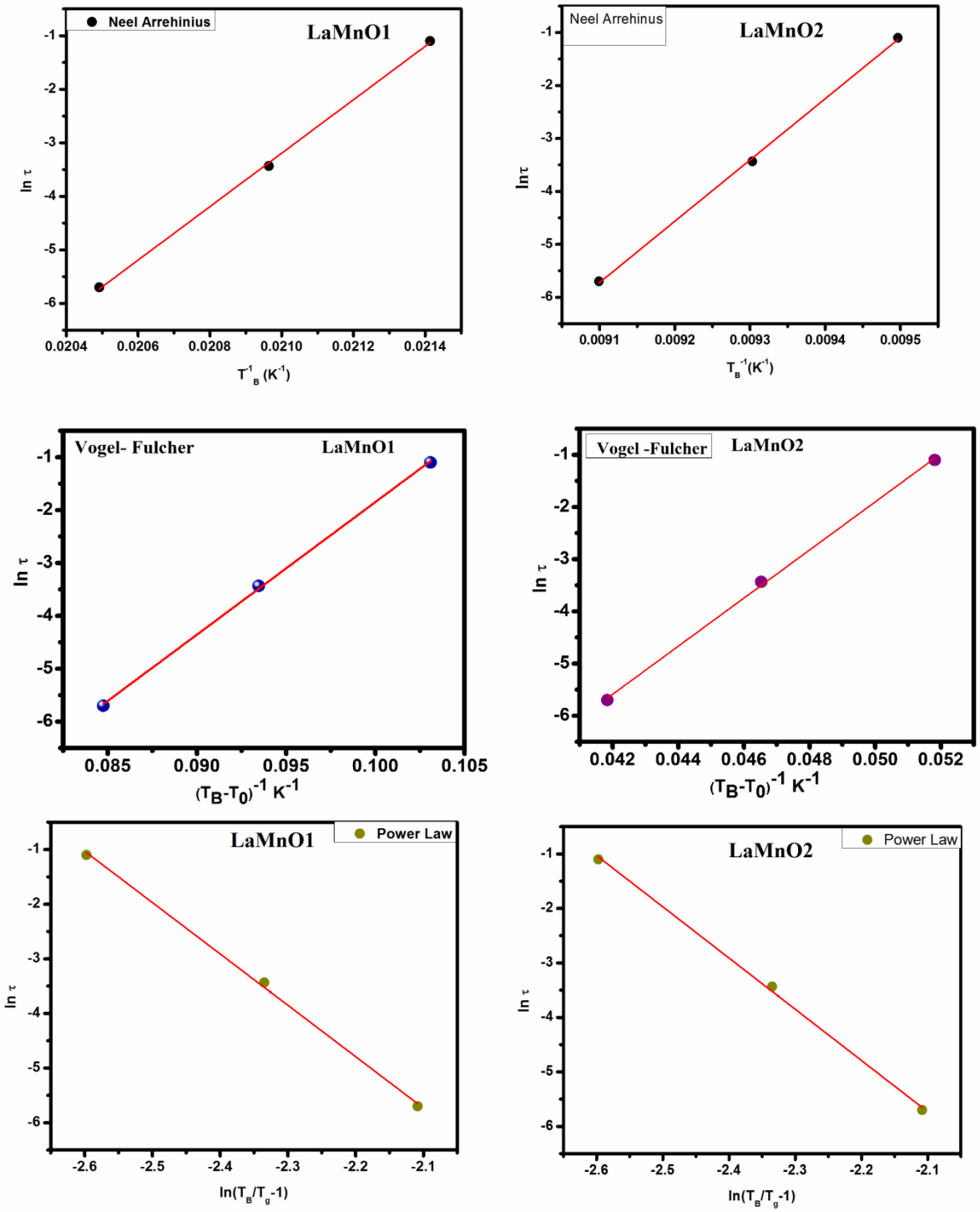

Figure 6.9 *Variation of relaxation time (τ) with T plotted with Neel-Arrehinius, Vogel-Fulcher and the Power law fitting for LaMnO1 and LaMnO2. The solid line represents the fitting.*

Therefore, we express the interacting dynamics by the Vogel–Fulcher law given as

$$\tau_{=}\tau_0 \exp\left(\frac{-\mathrm{Ea}}{\mathrm{K_B}\ (\mathrm{T_B}-To)}\right) \quad \textbf{(6.4)}$$

where T_0 i.e. Vogel–Fulcher temperature, which is a measure of the strength of inter particle interaction and has a value between 0 and T_B. The fitted data are shown in **Figure 6.9**. The parameters T_0, τ_0 and E_a/K_B are obtained by fitting Eq. **(6.4)** to ln τ vs $(T_B - T_0)^{-1}$, specified in **Table 6.3**. The τ_0 found to be within 10^{-11}–10^{-12} s cancel out the cluster-glass behavior because τ_0 in cluster glass is in the range of 10^{-6}–10^{-10} s. Thus it may be a match for the spin glass system where τ_0 is typically in the range 10^{-11} to 10^{-13} s [121]. For further confirmation of spin glass, the frequency dependent shift of the χ' peak is fitted with the Power law. According to Power law, the relaxation time (τ) is related to the correlation length (ξ) near the glass transition temperature (T_g). As ξ diverges at T_g, the relaxation time obeys the following empirical relation

$$\tau = \tau_0\left(\frac{\mathrm{T_B}}{\mathrm{T_g}} - 1\right)^{-z\upsilon} \quad \textbf{(6.5)}$$

$$\ln\tau = \ln\tau o - z\upsilon \ln\left(\frac{\mathrm{T_B}}{\mathrm{T_g}} - 1\right) \quad \textbf{(6.6)}$$

where z is the critical exponent related to the υ, z is the dynamic scaling exponent and T_g is the spin-glass transform temperature in the limit of zero frequency. Fitting the above equation as $\ln[(T_B/T_g)-1]$ versus ln τ are shown in **Figure 6.9**. The obtained parameters from the fit of the above equation are mention in **Table 6.3**. The values of τ_0 is well within the reported value for spin-glass (10^{-11}–10^{-13} s) and exponent zυ are found to be in the range of the reported value for spin-glasses (2– 10) and in both samples. Thus, we conclude that the LaMnO1 and LaMnO2 samples although show monoclinic phase, J-T distortion

decides the Curie temperature and effective magnetic moment is controlled by oxygen vacancies.

Table 6.3 Fitting parameters deduced from ac susceptibility fitted with different empirical relations like the Neel–Arrhenius, Vogel–Fulcher and Power law.

Sample Name	**Neel Arrhenius**		**Vogel-fulcher**			**Power Law**		
	E_a(eV)	**τ_o (sec)**	**T_o**	**E_a/K_B (eV)**	**τ_o (sec)**	**T_g(K)**	**zʊ**	**τ_o (sec)**
LaMnO1	0.4	1.20×10^{-47}	37	250.67	2×10^{-12}	32	8.7	7.4×10^{-13}
LaMnO2	0.9	6×10^{-49}	86	461.05	1.45×10^{-11}	98	9.4	8.6×10^{-12}

6.4 Conclusions

In this work, we demonstrated that monoclinic phase of $La_{1-x}MnO_3$ (x=0 and 0.2) could be achieved within a range of x varying from 0 to 0.2 synthesized through simple, cost effective co-precipitation technique. Rietveld refinement of X-ray diffraction pattern at room temperature pointed towards monoclinic distortion causing buckling and tilting of MnO_6 octrahedra, evidenced from the Mn-O-Mn bond angle and Mn-O bond length. FESEM analysis combined with crystallite size calculated from XRD peak profile confirmed the particles are of nanosize and polycrystalline in nature. While Curie temperature of the LaMnO1 and LaMnO2 samples are 124 K and 219 K respectively, the effective magnetic moment is high in the former sample than the later $LaMnO_3$ due to the presence of more oxygen vacancies evidenced from XPS analysis. The investigation of frequency dependent ac susceptibility after fitting with Neel–Arrhenius, Vogel–Fulcher and Power law, while canonical spin-glass, cluster-glass and interacting superparamagnetism

nature were cancelled out, both samples showed conventional spin glass behavior with a higher relaxation time in the LaMnO2.